MATERIALS SCIENCE

Bragg coherent diffractive imaging of single-grain defect dynamics in polycrystalline films

Allison Yau,[1] Wonsuk Cha,[2,3] Matthew W. Kanan,[1] G. Brian Stephenson,[2]* Andrew Ulvestad[2]*

Polycrystalline material properties depend on the distribution and interactions of their crystalline grains. In particular, grain boundaries and defects are crucial in determining their response to external stimuli. A long-standing challenge is thus to observe individual grains, defects, and strain dynamics inside functional materials. Here we report a technique capable of revealing grain heterogeneity, including strain fields and individual dislocations, that can be used under operando conditions in reactive environments: grain Bragg coherent diffractive imaging (gBCDI). Using a polycrystalline gold thin film subjected to heating, we show how gBCDI resolves grain boundary and dislocation dynamics in individual grains in three-dimensional detail with 10-nanometer spatial and subangstrom displacement field resolution. These results pave the way for understanding polycrystalline material response under external stimuli and, ideally, engineering particular functions.

Elucidating the effects of grain heterogeneity and defects on the properties of polycrystalline materials (*1*) is a topic of both scientific and technological importance, relevant to designing strain-tolerant materials (*2*, *3*), controlling ion intercalation (*4*, *5*), and designing new catalysts (*6*, *7*). Thus, much focus has been placed on understanding the links between the heterogeneous grain distribution, the motion of grain boundaries, and the resulting material properties. These ongoing developments have been driven in part by the ability to nondestructively determine the grain distribution and orientation by using x-ray diffraction (*8*, *9*), including advanced techniques such as micro-Laue (*10*, *11*) and high-energy diffraction microscopy (*12*, *13*). In particular, diffraction contrast tomography has been used to study grain growth (*8*, *14*). Electrons are also used in the form of electron backscatter diffraction (*15*) (EBSD) and electron microscopy (*16*, *17*). These techniques have made strides in correlating grain heterogeneity with material properties.

However, complete understanding at the atomic level of how grain boundaries and defects influence material properties requires the ability to image individual grains in polycrystalline materials during dynamic processes. Bragg coherent diffractive imaging (BCDI) is promising in this regard because it uses hard (~9 keV in this work) x-rays to obtain a three-dimensional (3D) image of the strain field in individual crystals. The primary difference between BCDI and other x-ray diffraction techniques is the ability to image the 3D strain and defect network in individual nanocrystals during different physical processes (*18*–*20*). A scanning version of the method known as ptychography was also used for 2D visualization of dislocations in silicon (*21*). BCDI was recently performed on an individual micrometer-sized grain, although specialized sample preparation was required and grain growth, grain boundary dynamics, and dislocation dynamics were not observed (*22*). Here we demonstrate 3D imaging of dislocation and grain morphology in sub–200-nm individual grains, which we denote as grain BCDI or gBCDI, in situ during heating. Using gBCDI, we show that dislocations can locally enhance grain growth and that coherent twin boundaries are very mobile during heating. gBCDI will likely find broad use in understanding the link between grains, their defects, and the properties of polycrystalline materials.

Gold thin films with a thickness of ~200 nm were synthesized by means of e-beam evaporation (*23*). In BCDI, the 3D intensity distributions around an isolated Bragg peak are collected by slightly rotating the crystal with respect to the incident x-ray beam (for example, cross sections from 3D data sets; see fig. S1.) In the past, observing isolated diffraction peaks from grains was challenging. By using a nonsymmetric scattering condition and a smaller beam, it was easy to find isolated, single-grain diffraction by translating the sample in the x-ray beam. The isolated 3D intensity distribution is then Fourier transformed into a real-space image after the phases are retrieved by using iterative algorithms (*23*–*27*). Real-space images of the Au grains were reconstructed with ~10-nm spatial resolution as determined by the phase retrieval transfer function (fig. S2). We first present results from an Au grain on a boron-doped diamond (BDD) substrate (fig. S3) that was imaged by using gBCDI during heating.

We determined the initial shape and size of a 200-nm-thick individual grain using an isosurface of the Bragg electron density (Fig. 1A). The grain had an orientation relative to the surface normal consistent with the electron microscopy image (fig. S4). The 3D information provided by gBCDI allows any cross section in the grain to be shown. We show both the amplitude (Fig. 1B) [proportional to the Bragg electron density (*28*)] and the phase (Fig. 1C) (proportional to the displacement field) at a cross section taken through the grain center. The grain has a low-amplitude region near the boundary and a spiral phase discontinuity at the same spatial location (both marked with white arrows on the image), which is the BCDI signature of a dislocation core (*20*, *29*).

We heated the sample (*23*) and imaged the grain multiple times at each temperature step (Fig. 2). Our heating procedure caused grain growth and improved faceting (Fig. 1, D to F). Growth and sharpening occurred nonuniformly in space, and much of the growth occurred near a previously identified dislocation (lower right corner in the 2D cross section, Fig. 1B). This region also had high surface curvature as judged by the rounded corner in the as-synthesized cross-section (Fig. 1B). The dislocation is absent in the 400°C image (Fig. 1E). Correlating the dislocation location with enhanced grain growth demonstrates a coupling of grain boundary mobility to intragrain dislocations.

One strength of our method is the ability to determine the time-dependent displacement field map that shows quantitative changes during the heating of our thin film (Fig. 2). The key insight we obtained from the correlation matrix (*23*) is that the displacement field changes slowly up through 300°C, and every scan is highly correlated, leading to the block-like structure. Because the film was previously annealed at 200°C for 30 min, we did not expect large changes up to this temperature. The large change at 400°C is due to the dislocation annihilation and corresponding grain growth (Fig. 1). This finding is consistent with the hypothesis that grain growth in nanocrystalline materials is limited until the temperature exceeds one-half of the melting point (*30*, *31*). Finally, at 400°C, the high correlation between displacement fields indicates that the grain boundary motion has stagnated, consistent with grain growth stagnation in pure materials (*32*).

We mapped the dislocation line in 3D using a gradient-based method (*20*, *29*) to determine the location where the dislocation terminated on the surface. Dislocation termination points can play important roles in, for example, crystal growth (*29*, *33*). We found that the dislocation line follows a horseshoe-like path in which the line originates near the grain boundary, then continues into the grain (extending ~40 nm inside) before turning and ultimately terminating at the grain

[1]Department of Chemistry Stanford University, Stanford, CA 94305, USA. [2]Materials Science Division, Argonne National Laboratory, Argonne, IL 60439, USA. [3]Advanced Photon Source, Argonne National Laboratory, Argonne, IL 60439, USA.
*Corresponding author. Email: gbs@anl.gov (G.B.S.); aulvestad@anl.gov (A.U.)

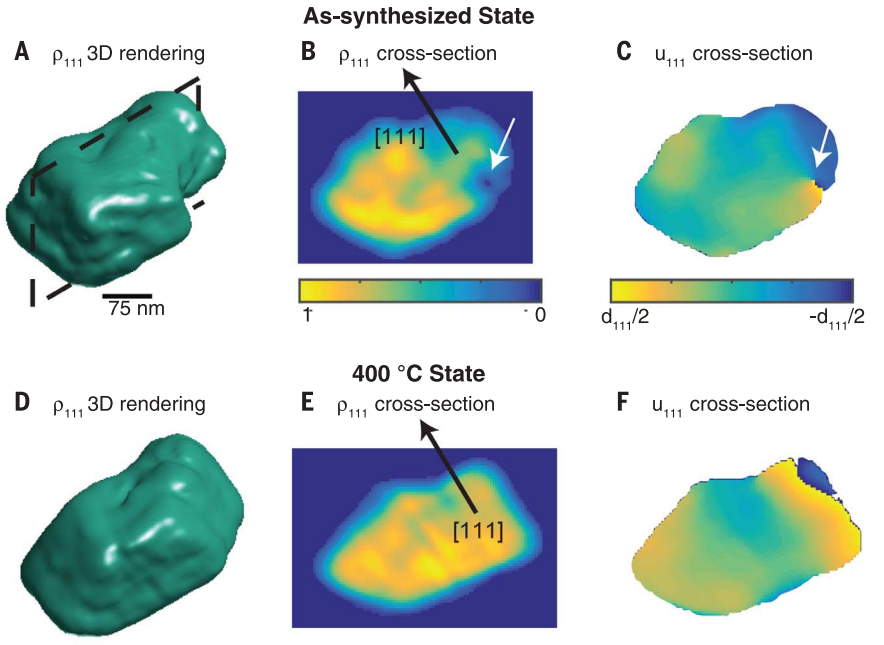

Fig. 1. Grain boundary and dislocation movement in a single gold grain during heating. (**A**) A 3D rendering of the reconstructed grain image; (**B**) cross-section view [cross-section location shown by the black dashed line in (A)] of the reconstructed Bragg electron density; and (**C**) cross-section view of the reconstructed displacement field for the as-synthesized state. The black arrow is the [111] scattering vector that is normal to a {111} facet. The white arrows show a low-amplitude region in the Bragg electron density and a corresponding discontinuity in the displacement field, which is consistent with a dislocation. (**D** to **F**) The same as in (A) to (C) but at 400°C. Grain growth, particularly near the dislocation, has occurred. The dislocation is absent.

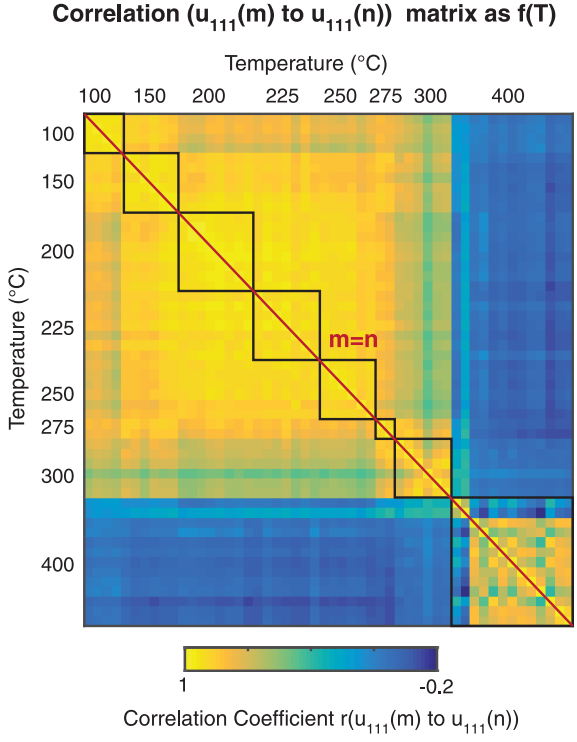

Fig. 2. Correlation dynamics during heating. The correlation matrix in which $r(u_{111}(m)$ to $u_{111}(n))$ is the Pearson r correlation coefficient between two different displacement fields $u_{111}(m)$ and $u_{111}(n)$. The matrix contains the computed r values for all possible combinations of the displacement fields measured while heating the grain up to 400°C. The temperature steps are 100°, 150°, 200°, 225°, 250°, 275°, 300°, and 400°C. The temperature at which each individual displacement field was measured is shown in the matrix. By definition, the matrix is symmetric and has a value of 1 along the diagonal (red line) where $m = n$ because every displacement field identically correlates with itself. The black boxes show the repeated measurements made at the same temperature. The largest change, as determined by the drop in correlation, occurred after heating to 400°C.

surface at a different location ~35 nm away (fig. S5A). Although this type of dislocation line is consistent with mixed dislocation loops that make 90° turns by transitioning from edge to screw dislocations (or vice versa) (*34*), exact identification would require measuring multiple Bragg peaks (*18*). The dislocation line is found up to and including the 300°C state and is not found at 400°C (fig. S5, B and C).

Grain microstructure, including the types and distributions of grain boundaries, plays an integral role in the bulk properties (*35*, *36*). To investigate coherent twin boundaries (CTBs), we made gBCDI measurements on SiO_2. Whereas the films on BDD were randomly oriented (fig. S6A), the films on SiO_2 were highly (111) textured (fig. S6B), and many of the imaged grains contained CTBs.

The cross section of the reconstructed Bragg electron density of a grain on a SiO_2 substrate at 500°C showed regions with the height of the film thickness that have large gaps in between the positive density regions (Fig. 3A). The boundary between the grain and the gap shows minimal displacement field variation, consistent with small strain and the sharing of atomic planes at that boundary (Fig. 3B). This type of image is consistent with CTBs observed by transmission electron microscopy (TEM) to have a low defect density at their boundaries (*37*). In a CTB, the twin and the parent crystal share a lattice plane but have mirrored stacking orders. A twin in face-centered cubic (fcc)–structured Au has, for example, stacking sequence CBA, whereas the stacking sequence in the parent region is ABC. The mirror in the stacking sequence is not energetically costly but changes the orientation of the lattice planes with respect to the incident x-rays, causing their diffraction to be located at a different place in reciprocal space for certain choices of the scattering vector relative to the twin plane (Fig. 3C). Any CTB with a {111} direction that is not the (111) direction being measured can cause this. Furthermore, gBCDI determines the phase difference between domains of the same orientation. This phase difference can only have three values for CTBs (*28*), and so it is particularly diagnostic for their identification. EBSD maps of the Au films on SiO_2 further confirm this identification, as they show that many of the grains within the film contain CTBs (figs. S7 and S8).

We tracked a grain (Fig. 4) with many CTBs during the heating protocol. In contrast to the Au on BDD samples, this film was not previously heated to 200°C. Initially, the grain shows seven or eight distinct sections, all with the same orientation. As the temperature is increased, some sections grow and become sharper, whereas others are reduced in size. At 100°C, it appears that the largest initial grains grow larger, but this trend reverses at 200°C. Instead, the grains on the far right that were initially small have started to grow. Finally, we observed changes even from 400° to 500°C. The grain growth at lower temperature compared to the grain discussed in Figs. 1 and 2 is probably due to a combination of the smaller initial grain size (*38*),

the lack of a 30 min 200°C pre-anneal, and the different wetting characteristics of Au on SiO_2 versus BDD. We show six additional grains (four from Au on SiO_2 substrates and two from BDD substrates) both before and after the heating protocol (fig. S9) to demonstrate the robustness of this approach for tracking grains and their defects. We also compare a reconstructed image of a grain with CTBs to the same grain imaged by EBSD and electron microscopy to show the agreement between the two techniques (fig. S10). The reconstructed image converges to the same result when different numbers of generations are used (fig. S11). Finally, we have computed the initial and final dilatory strain distributions for the two grains discussed previously (fig. S12) (*23*).

Our results show an avenue for imaging intra- and intergrain defect dynamics induced by external stimuli (e.g., pressure, temperature stress) in reactive environments at the individual grain level. The gBCDI method can provide information important to many applications, including creep and fatigue, strengthening mechanisms, and in improving material properties for catalysis and solar cells.

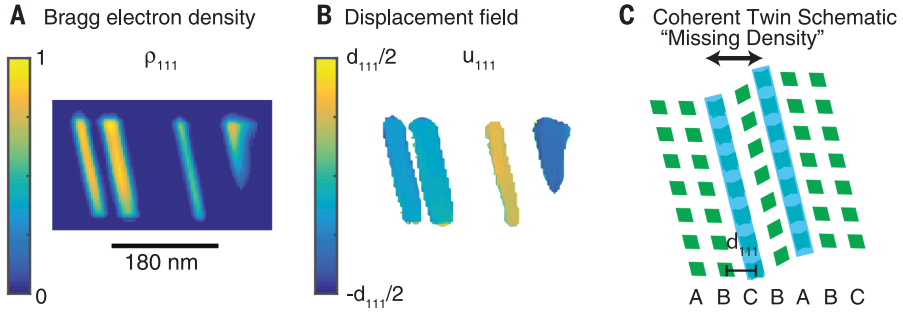

Fig. 3. Coherent twin boundaries in gold grains on SiO_2 substrates at 500°C. Cross sections of the Bragg electron density (**A**) and the displacement field (**B**) in the grain. The grain shows regions of zero density in between positive density regions. This density is physically present but is diffracting to a different reciprocal space location. Grains that share the same lattice as the parent crystal through coherent twin boundaries, which are shown schematically in (**C**), are prevalent owing to their low energy cost and are responsible for the zero-density regions. A mirror in the stacking sequence of the {111} planes causes the sequence of CBA to diffract at a different reciprocal space location from that of the ABC sequence. When the stacking reverts back to the original order, the lattice planes are exactly in registry with the original set and diffract to the same location.

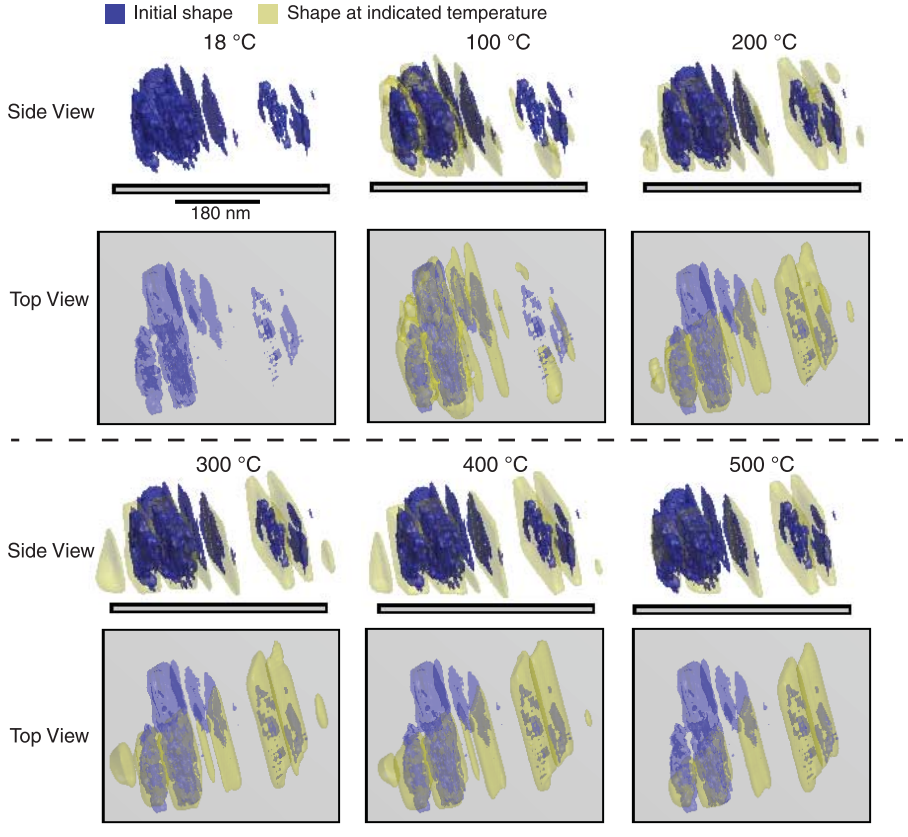

Fig. 4. 3D morphological evolution of a grain with many CTBs during heating. The initial grain shape is shown by a blue isosurface, whereas the shape at the indicated temperature is shown by a yellow isosurface. A side view and top view are shown. Grain boundary dynamics occur already at 100°C. The final state is correlated to the initial state, but the largest grains at 500°C are not the same as the largest grains at 18°C.

REFERENCES AND NOTES

1. M. Ashby, H. Shercliff, D. Cebon, *Materials: Engineering Science Processing and Design* (Butterworth-Heinemann, Oxford UK, 2007).
2. X. Zhang *et al.*, *Acta Mater.* **52**, 995–1002 (2004).
3. G. Gaucherin, F. Hofmann, J. P. Belnoue, A. M. Korsunsky, *Procedia Eng.* **1**, 241–244 (2009).
4. C. Lemier, J. Weissmüller, *Acta Mater.* **55**, 1241–1254 (2007).
5. N. Balke *et al.*, *Nat. Nanotechnol.* **5**, 749–754 (2010).
6. S. Xie, Q. Xu, X. Huang, *ChemCatChem* **8**, 480–485 (2016).
7. X. Feng, K. Jiang, S. Fan, M. W. Kanan, *J. Am. Chem. Soc.* **137**, 4606–4609 (2015).
8. W. Ludwig *et al.*, *Mater. Sci. Eng. A* **524**, 69–76 (2009).
9. M. Holt, R. Harder, R. Winarski, V. Rose, *Annu. Rev. Mater. Res.* **43**, 183–211 (2013).
10. F. Hofmann *et al.*, *Mater. Lett.* **64**, 1302–1305 (2010).
11. R. Spolenak *et al.*, *Phys. Rev. Lett.* **90**, 096102 (2003).
12. L. Renversade *et al.*, *IUCrJ* **3**, 32–42 (2016).
13. S. F. Li, R. M. Suter, *J. Appl. Cryst.* **46**, 512–524 (2013).
14. S. E. Offerman *et al.*, *Science* **298**, 1003–1005 (2002).
15. A. J. Schwartz, M. Kumar, B. L. Adams, D. P. Field, *Electron Backscatter Diffraction in Materials Science* (Springer, 2009), vol. 2.
16. B. Feng *et al.*, *Sci. Rep.* **6**, 20288 (2016).
17. B. Gao *et al.*, *Nanotechnology* **22**, 205705 (2011).
18. M. C. Newton, S. J. Leake, R. Harder, I. K. Robinson, *Nat. Mater.* **9**, 120–124 (2010).
19. I. Robinson, R. Harder, *Nat. Mater.* **8**, 291–298 (2009).
20. A. Ulvestad *et al.*, *Science* **348**, 1344–1347 (2015).
21. Y. Takahashi *et al.*, *Phys. Rev. B* **87**, 121201 (2013).
22. N. Vaxelaire *et al.*, *Acta Mater.* **78**, 46–55 (2014).
23. Materials and methods are available as supplementary materials.
24. Y. Shechtman *et al.*, Phase retrieval with application to optical imaging. arXiv:1402.7350 [cs.IT] (28 February 2014).
25. J. R. Fienup, A. M. Kowalczyk, *J. Opt. Soc. Am. A* **7**, 450 (1990).
26. S. Marchesini, *Rev. Sci. Instrum.* **78**, 011301 (2007).
27. J. R. Fienup, *Appl. Opt.* **21**, 2758–2769 (1982).
28. A. Ulvestad, J. N. Clark, R. Harder, I. K. Robinson, O. G. Shpyrko, *Nano Lett.* **15**, 4066–4070 (2015).
29. J. N. Clark *et al.*, *Nat. Mater.* **14**, 780–784 (2015).
30. C. L. De Castro, B. S. Mitchell, *Mater. Sci. Eng. A* **396**, 124–128 (2005).
31. H. Gleiter, *Acta Mater.* **48**, 1–29 (2000).
32. E. A. Holm, S. M. Foiles, *Science* **328**, 1138–1141 (2010).
33. F. C. Frank, *Discuss. Faraday Soc.* **5**, 48–54 (1949).
34. D. Hull, D. J. Bacon, *Introduction to Dislocations* (Butterworth-Heinemann, ed. 5, 2011).

35. V. E. Borthwick, S. Schmidt, S. Piazolo, C. Gundlach, *Geochem. Geophys. Geosyst.* **13**, Q05005 (2012).
36. D. L. Olmsted, E. A. Holm, S. M. Foiles, *Acta Mater.* **57**, 3704–3713 (2009).
37. J. R. Greer, *Nat. Mater.* **12**, 689–690 (2013).
38. S. Simões, R. Calinas, M. T. Vieira, M. F. Vieira, P. J. Ferreira, *Nanotechnology* **21**, 145701 (2010).

ACKNOWLEDGMENTS

This research used resources of the Advanced Photon Source, a U.S. Department of Energy (DOE) Office of Science User Facility operated for the DOE Office of Science by Argonne National Laboratory under Contract DE-AC02-06CH11357. This work was supported by U.S. DOE, Basic Energy Sciences, Materials Sciences and Engineering Division (gBCDI technique and analysis), and by the National Science Foundation CHE-1565945 (sample synthesis, electron microscopy). The data reported in this paper are archived at Beamline 34-ID-C at the Advanced Photon Source at Argonne National Lab and are available upon request. All code, including the reconstruction algorithm, is also available upon request. A.Y., W.C., and A.U. designed and performed the BCDI experiment. A.Y. synthesized the samples. All authors interpreted the results and contributed to writing the manuscript.

SUPPLEMENTARY MATERIALS

www.sciencemag.org/content/356/6339/739/suppl/DC1
Materials and Methods
Figs. S1 to S12
References (*39*–*45*)

16 December 2016; accepted 30 March 2017
10.1126/science.aam6168

Bragg coherent diffractive imaging of single-grain defect dynamics in polycrystalline films

Allison Yau, Wonsuk Cha, Matthew W. Kanan, G. Brian Stephenson and Andrew Ulvestad

Science **356** (6339), 739-742.
DOI: 10.1126/science.aam6168

Watching defects in heated thin films

The response of materials to external conditions depends on small-scale features such as defects and grain boundaries. Yau *et al.* heated gold thin films and used coherent x-ray diffractive imaging to track how these microstructures developed during grain growth (see the Perspective by Suter). The technique allowed nondestructive visualization of the features in three dimensions. The method should help link external stimuli to material response through changes in microstructure, thereby allowing development of novel materials through microstructural engineering.

Science, this issue p. 739; see also p. 704